

# ACCEPTED VERSION

Matthew J. Emes, Azadeh Jafari, Maziar Arjomandi

**A feasibility study on the application of mesh grids for heliostat wind load reduction**  
Solar Energy, 2022; 240:121-130

© 2022 International Solar Energy Society. Published by Elsevier Ltd. All rights reserved.

This manuscript version is made available under the CC-BY-NC-ND 4.0 license  
<http://creativecommons.org/licenses/by-nc-nd/4.0/>

Final publication at: <http://dx.doi.org/10.1016/j.solener.2022.05.033>

## PERMISSIONS

<https://www.elsevier.com/about/policies/sharing>

Accepted Manuscript

Authors can share their [accepted manuscript](#):

24 Month Embargo

**After the embargo period**

- via non-commercial hosting platforms such as their institutional repository
- via commercial sites with which Elsevier has an agreement

**In all cases [accepted manuscripts](#) should:**

- link to the formal publication via its DOI
- bear a CC-BY-NC-ND license – this is easy to do
- if aggregated with other manuscripts, for example in a repository or other site, be shared in alignment with our [hosting policy](#)
- not be added to or enhanced in any way to appear more like, or to substitute for, the published journal article

**13 August 2024**

<http://hdl.handle.net/2440/135519>

# A feasibility study on the application of mesh grids for heliostat wind load reduction

Matthew J. Emes<sup>\*1</sup>, Azadeh Jafari<sup>1</sup>, Maziar Arjomandi<sup>1</sup>

<sup>1</sup> Centre for Energy Technology, School of Mechanical Engineering, The University of Adelaide, SA 5005, Australia

## Abstract

This study examines the effectiveness of mesh grids in heliostat field perimeter fences and edge-mounted devices for heliostat wind load reduction. Two experimental studies were conducted: (1) the effect of mesh porosity and non-dimensional longitudinal distance of a perimeter fence upstream on the forces on a heliostat, and (2) the effect of mesh porosity and non-dimensional height-chord ratio of a heliostat edge-mounted mesh device on the heliostat loads. The experiments were conducted using an instrumented heliostat model positioned in the atmospheric test section of the Adelaide Wind Tunnel. It was found that perimeter mesh fences reduce peak loads by up to 50% and edge-mounted porous mesh devices reduce peak loads by up to 30% at the expense of increasing loads at different elevation angles. The porosity and height-chord ratio of an edge-mounted mesh were found to be important parameters influencing the maximum drag and lift reductions in operating and stow positions. The results of this work show the potential of mesh grids for reducing wind load on heliostats, and the importance of conducting a detailed techno-economic analysis on mesh grids throughout a heliostat field. The application of mesh grids on commercial-scale heliostats requires a further evaluation of the reduction of heliostat wind loads and thus cost of a field through mitigation of the incoming ABL turbulence and wake-induced turbulence from upstream heliostats.

**Keywords:** mesh; fence; porosity; heliostat; drag; lift

## Nomenclature

$A$	Heliostat panel area = $c^2$ (m <sup>2</sup> )
$\alpha$	Heliostat elevation angle (°)
$\beta$	Heliostat azimuth angle (°)
$c$	Heliostat panel chord length (m)
$c_{Fx}$	Coefficient of drag force

28	$c_{Fz}$	Coefficient of lift force
29	$F_x$	Drag force (N)
30	$F_z$	Lift force (N)
31	$f$	Frequency (Hz)
32	$H$	Height of the porous mesh perimeter fence (m)
33	$h$	Height of the heliostat edge-mounted porous mesh device (m)
34	$I_u$	Longitudinal component of turbulence intensity
35	$I_w$	Vertical component of turbulence intensity
36	$L_u$	Longitudinal component of integral length scale (m)
37	$L_w$	Vertical component of integral length scale (m)
38	$\rho$	Air density (kg/m <sup>3</sup> )
39	$p$	Pressure (Pa)
40	$U_\infty$	Freestream wind speed (m/s)
41	$x$	Longitudinal distance from the porous mesh perimeter fence (m)
42	$x_h$	Longitudinal distance from the heliostat (m)
43	$y$	Lateral distance (m)
44	$z$	Height above the ground at the position of the porous mesh perimeter fence (m)
45	$z_h$	Height above the ground at the position of the heliostat (m)
46	$z_0$	Logarithmic roughness height (m)

## 47 1. Introduction

48 Wind loads impact the cost of heliostats through strength and stiffness considerations and local  
49 wind conditions for reliability, serviceability and durability of components over the design life of a  
50 concentrating solar power (CSP) central receiver plant (Emes *et al.* 2021). The growth of urban areas  
51 or changing vegetation, such as during the manufacturing and deployment of a heliostat field in a low-  
52 roughness environment, can lead to larger wind loads on structural components and increase the  
53 manufacturing cost of heliostats (Emes *et al.* 2020). Hence, reduction of the wind loads on the heliostat  
54 field is crucial to lower the total heliostat cost to \$50/m<sup>2</sup> (Department of Energy 2017) and decrease the  
55 levelised cost of electricity (LCOE) of CSP with thermal energy storage to be a competitive energy  
56 source with solar PV and wind. The drag and lift forces and their non-dimensional aerodynamic  
57 coefficients are used in the wind load design of heliostats. The maximum drag force occurs at large  
58 elevation angles representing an upright orientation with increased cross-sectional area to the flow. The  
59 lift force is significant at small elevation angles and in stow position due to high-pressure differences  
60 along the heliostat surface. The maximum wind loads are strongly correlated to turbulence within the

atmospheric boundary layer (ABL) wind flow approaching a heliostat field (Peterka *et al.* 1989; Pfahl *et al.* 2015; Emes *et al.* 2020).

Wind load reduction can be achieved through the mitigation of moderate to high levels of turbulence in the approaching ABL. A possible method for suppression of ABL turbulence is the application of wind barriers, such as fences around the perimeter of a heliostat field. The wind loads on heliostats in subsequent rows of a field relative to an isolated heliostat have previously been reported as a function of the ratio of the projected blockage area of upstream obstacles to ground area (Peterka *et al.* 1986; Pfahl 2018). However, the blockage generated by the fence and the upstream heliostats were not independently reported in these wind tunnel studies. A single mesh fence with porosity, defined as the ratio of open area to total fence area, of 0.46 reduced the longitudinal turbulence intensity of the incoming ABL from 12.5% to 9% and reduced the integral length scale by 25% at a distance of two fence heights downstream of the fence (Jafari *et al.* 2021). The longitudinal turbulence component mainly impacts the drag force coefficient (Emes *et al.* 2020), whereas the vertical component of turbulence is correlated to the peak lift force coefficient in stow position (Jafari *et al.* 2019). However, the variation of heliostat wind loads behind a mesh fence with different grid parameters at a range of downstream distances has not been investigated. The first objective of this study is therefore to characterise the effect of mesh scaling parameters of a perimeter fence on its wake turbulence characteristics and heliostat wind loads downstream of the fence.

Despite the deployment of perimeter fences for protection of solar fields, their manufacturing cost increases with increasing heliostat size. A potential alternative to a perimeter fence is to manipulate the flow field approaching to individual heliostats by attaching small sections of a mesh structure onto the edge of a heliostat as a turbulence reduction method for in-field heliostats. Wind loads in stow position were reduced by 40% through application of mesh grids mounted along the edges of a heliostat model (Pfahl *et al.* 2014). The edge-mounted mesh grids reduced vortex shedding from the heliostat and flow separation that yielded a 30% reduction in the support structure weight (Pfahl *et al.* 2014). However, insufficient detail of the test conditions and the mesh geometry parameters leading to load reduction in stow position was provided. The porosity is a critical geometric parameter of a mesh that governs the downstream flow behaviour, followed by the mesh height, hole size and hole geometry (Li and Sherman

2015). Below a critical porosity in the range of 0.3-0.4, a mesh behaves similarly to a solid wall causing large regions of flow separation (Perera 1981). To attenuate incoming turbulent flow downstream, mesh fences are commonly designed with a porosity greater than these critical values in the medium porosity range. With increasing height of a mesh, it becomes more effective at shielding the leeward regions with reduced wind speed and unsteadiness in the velocity fluctuations. The height of a mesh influences the distance behind the fence that is sheltered from incoming turbulent flow. The drag and lift forces on the heliostat structure are influenced by the pressure distribution over the flat heliostat surface. Mesh grids significantly impact the amplitude of unsteady wind components and thus can reduce the peak forces. With decreasing porosity of a mesh, increasing pressure drop causes a larger reduction in mean forces but increased surface area of the mesh leads to larger bluff body drag. Porous mesh treatments on the leading edge of a NACA 5406 airfoil reduce lift force by 23% relative to a solid leading edge by reducing the peak pressure coefficient on the suction side of the airfoil. However, a porous edge treatment causes drag force increases of 30% and 55% on NACA 0012 and 5406 airfoils, respectively, due to the enhancement of flow instability in the boundary layer on the suction side and increase in momentum thickness (Teruna *et al.* 2021). A porous mesh edge attachment on the leading edge of a heliostat offers a potential to attenuate incoming ABL turbulent eddies impinging on the heliostat and thus reduce separation and resultant lift forces. The second objective of this study is therefore to investigate the scaling parameters including porosity and height of an edge-mounted mesh device that influence the wind load reduction on stow and operating heliostats at different elevation angles.

This paper aims to investigate perimeter fences which affect the flow field approaching heliostat field and edge-attachment meshes which change the flow field to which individual heliostats are exposed, with an ultimate objective to determine the optimal geometric mesh parameters, including their height, porosity, and distance with respect to the heliostat to reduce the wind loads at different elevation angles. To achieve these objectives a heliostat instrumented with load cells and mesh devices was tested in the University of Adelaide boundary layer wind tunnel. The establishment of correlations between in-field flow turbulence and heliostat load distributions and their dependence on mesh device scaling parameters allows for the heliostat field layout and structural design to be optimised with respect to the wind loads. Development of such relationships is crucial to better understand the dynamic wind

effects on heliostats in different positions of a field and further reduce the cost of structural wind-resistant components.

## 2. Methodology

Experiments were conducted in the atmospheric test section of  $3\text{ m} \times 3\text{ m}$  cross-section and 17 m development length in the University of Adelaide wind tunnel. The atmospheric boundary layer (ABL) was generated in the wind tunnel using a set of truncated spires and surface roughness elements, as shown in Figure 1. Five spires of 1.3 m height and 0.155 m base width were placed with their centrelines separated by lateral distances of 0.5 m. Following the spires, a fetch of roughness elements spanned the tunnel over a streamwise length of 7.2 m. The roughness elements of  $90\text{ mm} \times 90\text{ mm}$  cross-section and 45 mm height were placed in a staggered arrangement with approximately 24% coverage of the floor area. The details of the setup can be found in Jafari *et al.* (2021). Figure 2(a) shows the experimental setup with the perimeter fence upstream of the instrumented heliostat model mounted on a platform containing four load cells. Each three-axis load cell has 2 N range, with an accuracy of 0.5%. A data acquisition system was used to collect force data in the three orthogonal directions at a sampling rate of 1 kHz. Flow measurements were taken using a multi-hole pressure probe capable of measuring three velocity components with an accuracy of  $\pm 0.5\text{ m/s}$ . The heliostat model in Figure 2(b) with a scaling ratio of 1:60 consists of a pylon and a hinged flat plate panel with a chord length  $c = 0.2\text{ m}$ . In the first test, four fences of wire mesh type with porosities of 0.46, 0.56, 0.64 and 0.73 and a constant height of  $H = 0.4\text{ m}$  spanning the wind tunnel cross-section (Figure 2a) were investigated. A square heliostat model with chord length  $c = 0.2\text{ m}$  and hinge height of 0.15 m was placed on the load cell platform for force measurements at four different distances downstream of the fences, varying between  $x/H = 1.5$  and  $x/H = 3.4$  in Figure 1. For the second test, a single mesh grid, with porosities of 0.46, 0.5 and 0.9 and mesh height  $h$  (relative to the heliostat plate with total height  $2h$  in Figure 2b) to heliostat chord ratios  $h/c = 0.1, 0.05$  and  $0.025$ , was attached to the leading edge of the heliostat on the force platform. Wake measurements were taken at three different distances downstream of the heliostat model, varying between  $x_h = 2$  and  $x_h = 4$  in Figure 1.

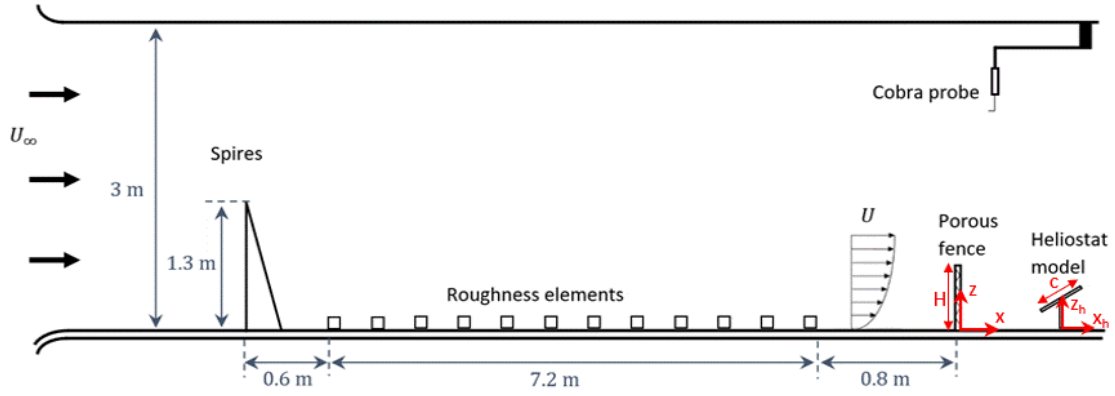


Figure 1. Schematic of the ABL with spires and roughness elements in the wind tunnel and coordinate systems of the porous fence and heliostat model.

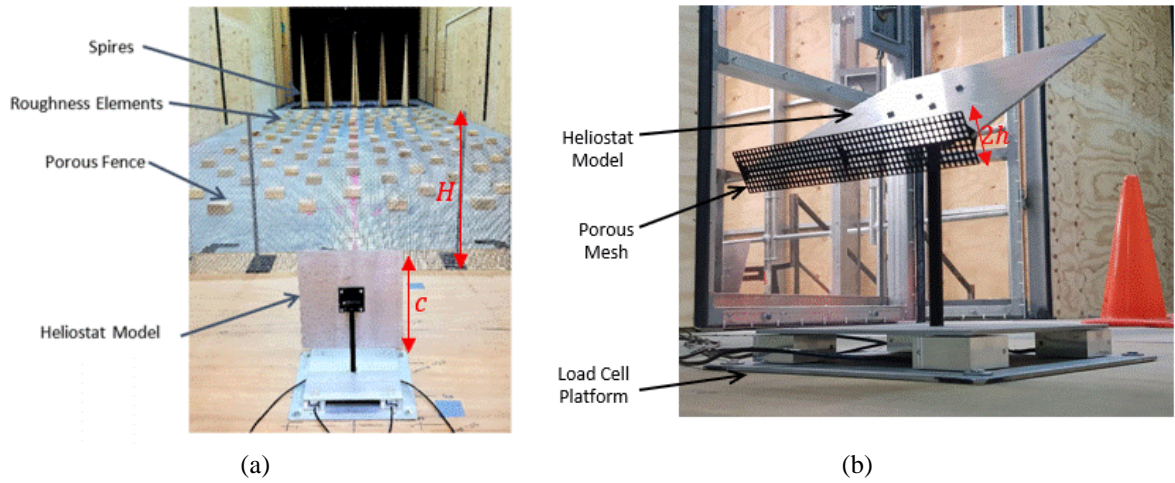


Figure 2. Generation of the ABL with spires and roughness elements in the wind tunnel: (a) perimeter fence of height  $H$  upstream of the instrumented heliostat model of chord length  $c$ , (b) edge-mounted mesh device of total height  $2h$  on the leading edge of the heliostat model mounted to the load cell platform.

Figure 3 shows the ABL profiles (non-dimensionalised with fence height  $H = 0.4$  m) of the mean velocity normalised with the freestream velocity  $U_\infty = 11$  m/s, and the turbulence intensities and integral length scales in the absence of the fence, which compared well with Jafari *et al.* (2021) for verification purposes. Figure 3(a) shows the mean velocity profile lies within  $\pm 1.5\%$  error range of the published data fitted to a logarithmic profile with  $z_0 = 0.002$  m (Jafari *et al.* 2021). The turbulence intensity profiles in Figure 3(b) lie within the typical range of low-roughness terrains, with the longitudinal  $I_u = 13\text{--}15\%$  and vertical  $I_w = 8\text{--}9\%$  at  $z = 0.15$  m (Jafari *et al.* 2021). The streamwise ( $L_u$ ) and vertical ( $L_w$ ) integral length scales in Figure 3(c) increase with increasing height and are reduced close to the ground, due to the constrained tunnel cross-section and development length (Jafari

*et al.* 2019). The scatter in the integral length scale profiles, particularly for the longitudinal component, results from anisotropic turbulence generated in the boundary layer wind tunnel. Despite the variation in the turbulence length scale profiles, the values are within an acceptable average error range of  $\pm 5\%$ .

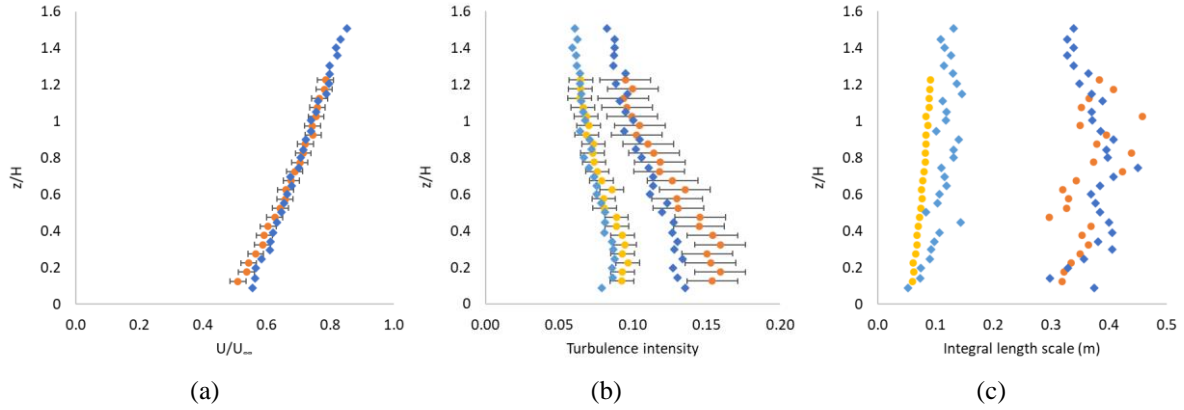


Figure 3. ABL profiles measured in the current study compared with Jafari *et al.* (2021): (a) mean velocity, (b) streamwise and vertical turbulence intensities, (c) streamwise and vertical integral length scales. Orange circles represent longitudinal velocity component profiles, yellow circles represent vertical velocity component profiles and error bars show the standard deviation of the measurements in the current study. Blue diamonds represent the corresponding profiles in Jafari *et al.* (2021).

### 3. Results and Discussion

To verify the conducted measurements on a single heliostat reference case without a mesh structure attached and without a perimeter fence, Figure 4 shows the three-sigma peak drag and lift coefficients at different elevation angles ( $\alpha$ ) compared with studies by Emes *et al.* (2019) and Peterka *et al.* (1989). A similar general trend is observed, where the drag coefficient increases with increasing elevation angle and the lift coefficient is largest at  $\alpha = 30^\circ$ . The largest differences between the studies are observed in stow position and at  $\alpha = 90^\circ$ . The peak drag coefficient in stow ( $\alpha = 0^\circ$ ) is 0.5 in the current study, compared to 0.4 in Emes *et al.* (2019) and 0.1 in Peterka *et al.* (1989). Similarly, the peak drag and lift coefficients at  $\alpha = 90^\circ$  lie between the previous studies, with the variations due to the effects of turbulence intensities (Peterka and Derickson 1992; Pfahl *et al.* 2015; Emes *et al.* 2017) and ratio of integral length scales to heliostat chord length (Emes *et al.* 2017; Emes *et al.* 2019; Jafari *et al.* 2019). Longitudinal turbulence intensities are in the range of 13-15% in the wind tunnel experiments shown in Figure 4. However, the effect of integral length scales is particularly relevant given the different heliostat model sizes with chord length  $c = 0.2$  m in the current study compared with 0.3 m in Peterka *et al.* (1989) and 0.8 m in Emes *et al.* (2019). This results in discrepancies between the ratio of the



turbulence length scales relative to the size of the heliostat (Emes *et al.* 2017; Emes *et al.* 2020). Differences in the heliostat elevation axis height to chord length ratio of 0.48 in Peterka *et al.* (1989), 0.63 in Emes *et al.* (2019) and 0.75 in the current study, and thus the ratio of the vertical distance from the lower heliostat edge to the ground and the chord length, are postulated to particularly impact the maximum drag coefficient at  $\alpha = 90^\circ$  and the maximum lift coefficient at small elevation angles but this requires further investigation. Nevertheless, the general similarity between the drag and lift coefficients in the different studies gives confidence of the accuracy of the results obtained in the current study. The results presented in the following sections are normalised against the reference case of a single unmodified heliostat (i.e. without a mesh structure attached and without a perimeter fence) in Figure 4.

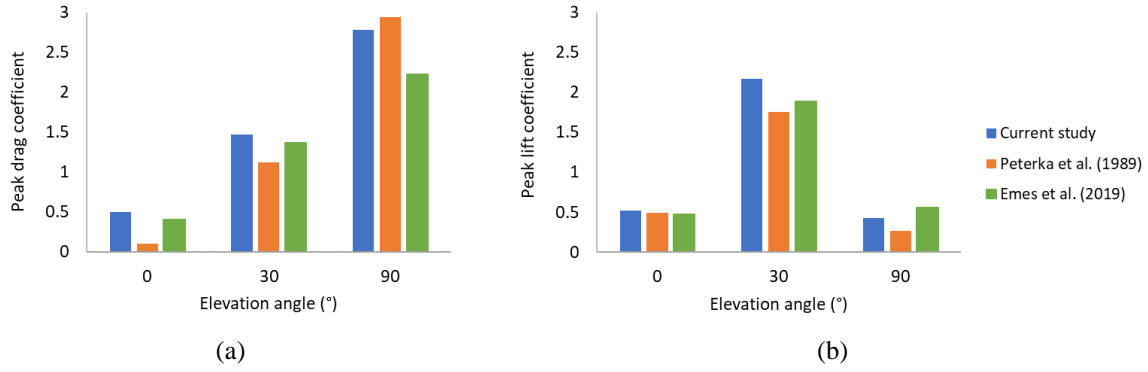


Figure 4. Comparison of peak load coefficients on a single unmodified heliostat with wind tunnel experiments (Peterka *et al.* 1989; Emes *et al.* 2019) as a function of elevation angle: (a) drag, (b) lift.

### 3.1. Perimeter fences

Figure 5 shows the effect of fence porosity on the turbulent flow profiles at a distance of  $x/H = 2.75$  downstream of the fence. Velocity and turbulence profiles have been normalised with their corresponding values measured in the absence of the fence (see Figure 3). As shown in Figure 5(a), the fences create a reduction in the mean velocity at height below  $z/H = 1.2$  with a larger reduction for a lower porosity fence. For instance, the fence with a porosity of 0.46 reduces the mean velocity by up to 25% while a porosity of 0.73 leads to a maximum of 12% reduction in the mean velocity. At heights of  $z/H > 1.2$ , there is a slight increase in mean velocity especially for low-porosity fences due to the flow being stagnated by the fence. Figure 5(b-c) show the effect of the fences on longitudinal ( $I_u$ ) and vertical ( $I_w$ ) turbulence intensity profiles. Both  $I_u$  and  $I_w$  are reduced downstream of the fences at  $z/H < 0.8$ ,

also with a larger reduction for lower porosities. The reduction in streamwise turbulence intensity is larger than vertical turbulence intensity as for example for a porosity of 0.46, the maximum reduction in  $I_u$  is 35% compared to 25% for  $I_w$ . Turbulence intensities increase significantly at  $z/H \approx 1$  due to flow separation at the fence top edge. To avoid increased turbulence intensities compared to the incoming flow, the fence height must therefore be larger than the heliostat with hinge height  $z_H/H = 0.375$  so that at all operating angles the heliostat is positioned at  $z/H < 0.8$ .

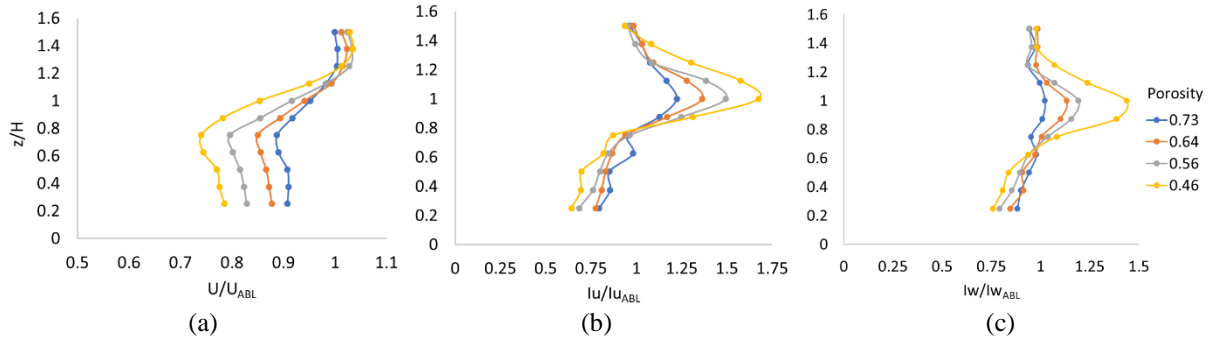


Figure 5. Effect of mesh fence porosity at  $x/H = 2.75$  on profiles of (a) mean velocity, (b) longitudinal turbulence intensity, (c) vertical turbulence intensity, normalised with respect to the incoming ABL profiles in Figure 3.

Figure 6(a-b) show the normalised peak loads on a heliostat downstream of a fence as a function of fence porosity and elevation angle. The load reductions are calculated from the measurement at a distance of  $x/H = 2.75$  downstream of the fence compared to the measured forces on a heliostat with no upstream fence. It is found that a lower porosity fence creates a larger reduction in peak drag and lift forces, which is associated with the larger velocity deficit and reduced turbulence intensities behind the low-porosity fence. The results show that the force reductions are a linear function of fence porosity in the measured range of porosities and do not vary with the operating elevation angle. As shown in Figure 6(a-b), a fence with a porosity of 0.46 reduces the peak drag and lift forces by 50% and 42% at all operating angles, respectively, and a fence with a porosity of 0.73 creates a reduction of approximately 25% and 20% in peak drag and lift forces. At  $\alpha = 0^\circ$  in Figure 6(b), the force reductions are between 55% and 25% for porosities between 0.46 and 0.75. The reduction is smaller in magnitude compared to the operating elevation angles, as the forces are directly proportional to the wind velocity squared. The smaller reduction of peak lift force at  $\alpha = 0^\circ$  is highly correlated with the vertical component of turbulence intensity behind the fence (Jafari *et al.* 2019).

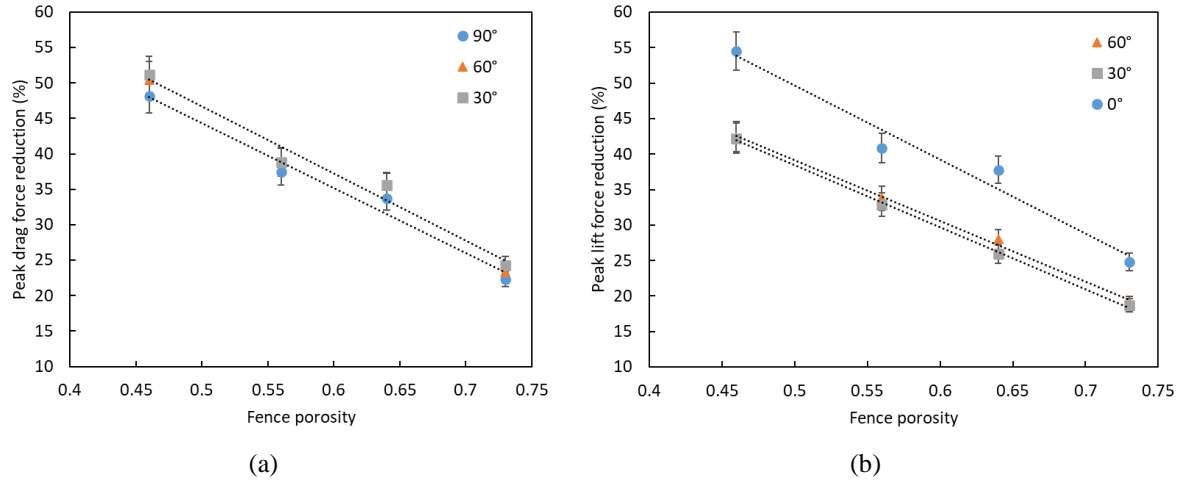


Figure 6. Effect of mesh fence porosity at  $x/H = 2.75$  on (a) drag and (b) lift forces on a heliostat downstream of the fence relative to those on an isolated heliostat at different elevation angles.

Figure 7 and Figure 8 show the drag and lift forces on a heliostat at  $\alpha = 30^\circ$  at different downstream distances from the fence,  $x/H$ , normalised with those on a heliostat in the absence of a fence. With the increase of the downstream distance, the reduction in drag forces and lift forces become smaller as the velocity and turbulence intensity start to recover to their undisturbed condition upstream of the fence. The results however show that at the furthest measurement location,  $x/H = 3.4$ , the flow has not yet recovered and therefore a wind load reduction is observed. For example, as shown in Figure 7(a) the normalised mean drag force behind a fence with a porosity of 0.46 changes from 0.52 at  $x/H = 1.5$  to 0.68 at  $x/H = 3.4$ . The reductions are smaller for a higher porosity fence, such as a 0.73 porosity fence produces a normalised mean drag force between 0.78 and 0.92 at  $x/H = 1.5$  and  $x/H = 3.4$ , respectively. A similar trend is observed for the mean and peak lift forces in Figure 8.

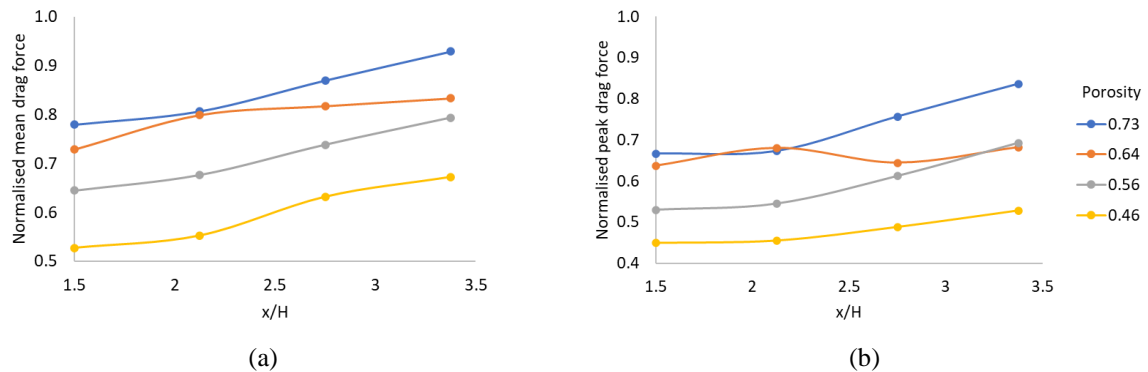


Figure 7. Normalised (a) mean drag force and (b) peak drag force relative to a heliostat with no fence as a function of mesh fence porosity and distance  $x/H$  downstream of the fence with height  $H$ .

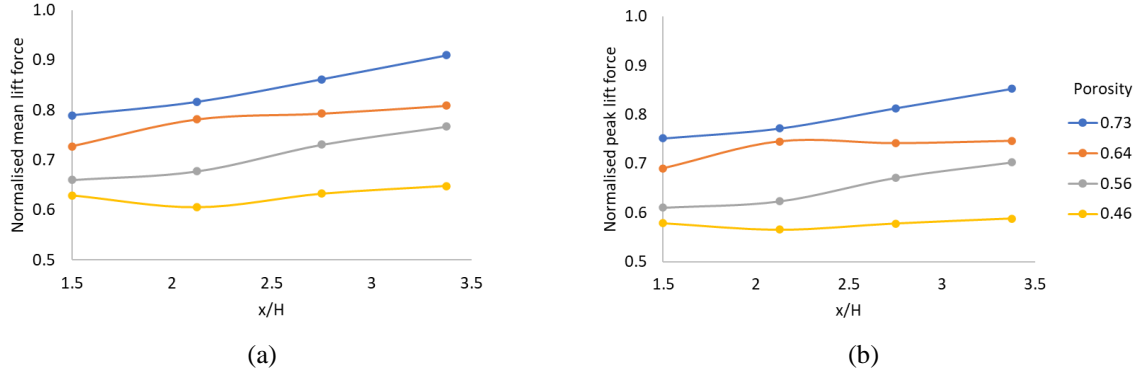


Figure 8. Normalised (a) mean lift force and (b) peak lift force relative to a heliostat with no fence as a function of mesh fence porosity and distance  $x/H$  downstream of the fence with height  $H$ .

### 3.2. Edge-mounted mesh devices

Figure 9 and Figure 10 show the variation of the mean velocity and turbulence intensity profiles, respectively, normalised with respect to the incoming ABL flow profiles in Figure 3 at distances  $x_h/c$  downstream of a single unmodified heliostat and a single heliostat with a 0.9 porosity mesh attachment on the leading edge at different elevation angles. At  $\alpha = 0^\circ$  in Figure 9(a-c) and at  $\alpha = 60^\circ$  in Figure 9(g-i), the heliostat with mesh edge attachment produces an additional 5-10% velocity deficit compared with the heliostat with no mesh edge attachment at heights below the heliostat elevation axis ( $z_h/c < 0.75$ ). This is due to the increased blockage effect of the mesh with increasing elevation angle as the orientation of the porous mesh is closer to perpendicular than parallel with the flow direction of the incoming ABL. The non-uniform velocity and vertical turbulence intensity profiles at  $x_h/c = 2$  in the near wake of the stowed heliostat recovers to an approximately uniform profile at  $x_h/c = 4$ . In contrast at  $\alpha = 30^\circ$  in Figure 9(d-f) and Figure 10(d-f), there is a modest increase in both profiles with the addition of the mesh. The porosity of the mesh leading edge attachment at elevation angles of  $30^\circ$  or lower reduces the blockage effect and enhances dissipation of small-scale eddies downstream of the heliostat. The effect of the edge-mounted mesh device on the unsteady component downstream flow profiles increases with increasing  $\alpha$ , such that the vertical turbulence intensity at  $x_h/c = 2$  increases by a magnitude of 3.5 times at  $\alpha = 30^\circ$  and 9 times at  $\alpha = 60^\circ$  compared with the incoming ABL. A faster recovery of the wake profiles is observed at  $\alpha = 60^\circ$  as the non-dimensional velocity decreases from 34% to 77% and non-dimensional turbulence intensity decreases from 8.7 to 3.6 with increasing downstream distance from  $x_h/c = 2$  to 4.

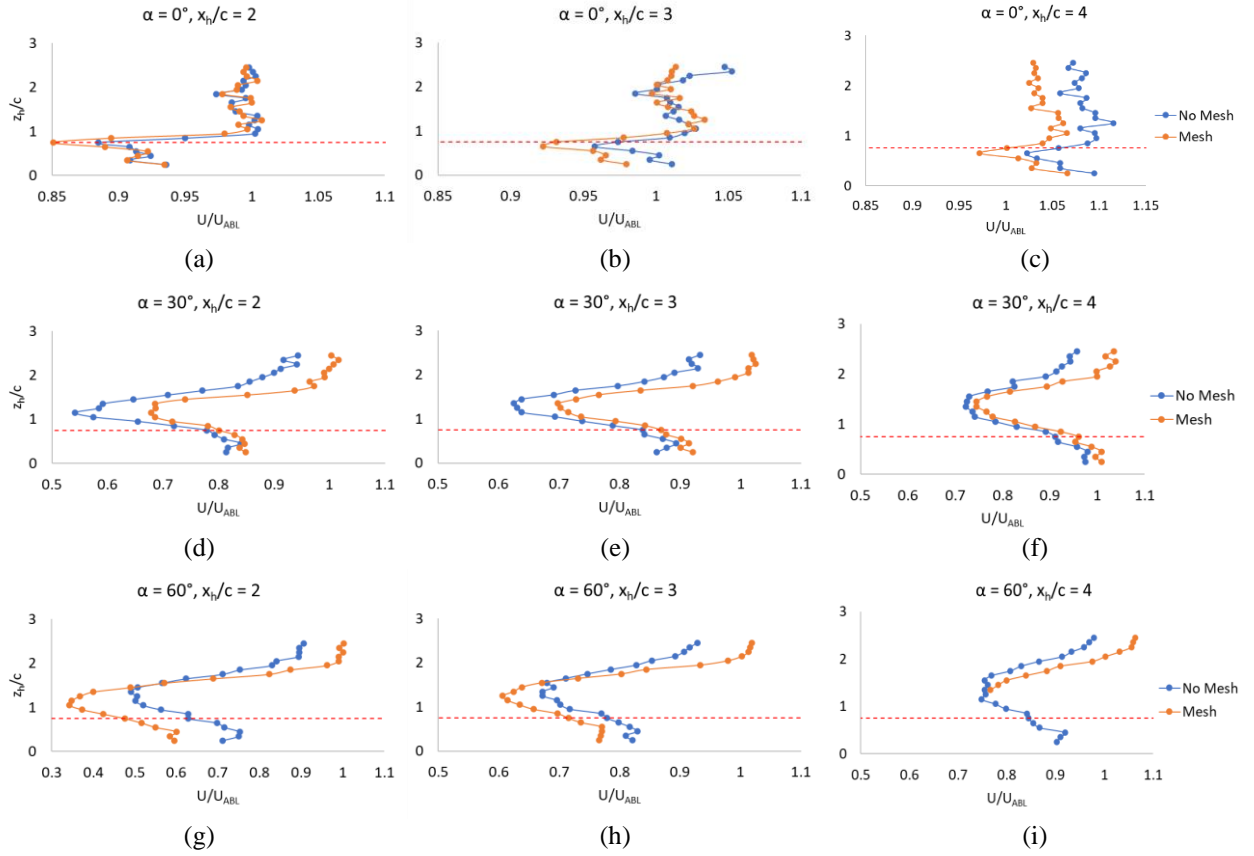
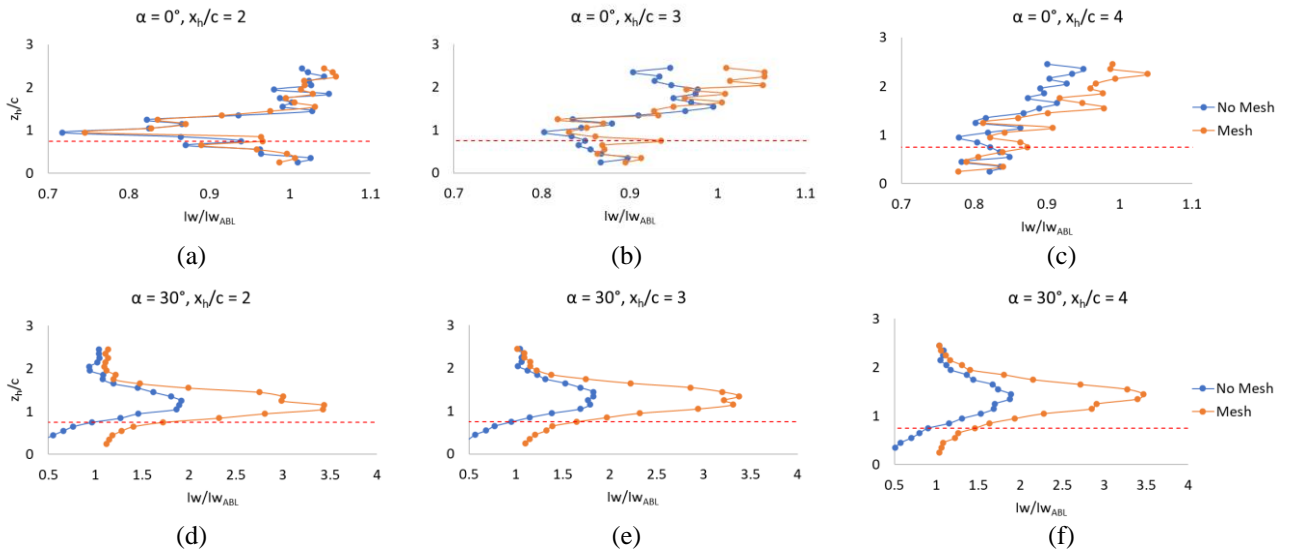


Figure 9. Effect of an edge-mounted mesh device with 0.9 porosity on mean velocity profiles normalised with respect to the incoming ABL flow, as a function of distance  $x_h/c$  from 2 to 4 downstream of a heliostat at elevation angle (a-c)  $\alpha = 0^\circ$ , (d-f)  $\alpha = 30^\circ$  and (g-i)  $\alpha = 60^\circ$ . Blue circles indicate the profiles in the wake of a single unmodified heliostat with no mesh and orange circles indicate the profiles in the wake of a single heliostat with a leading edge-mounted mesh device. The red dashed line indicates the heliostat hinge height  $z_h/c = 0.75$ .



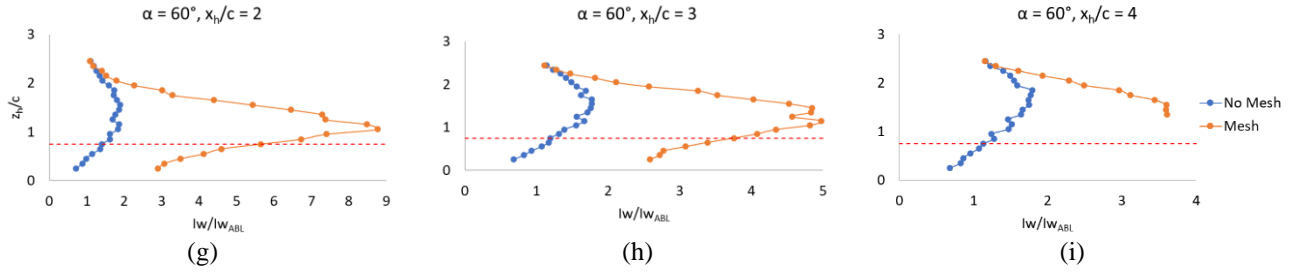


Figure 10. Effect of an edge-mounted mesh device with 0.9 porosity on vertical turbulence intensity profiles, normalised with respect to the incoming ABL flow, as a function of distance  $x_h/c$  from 2 to 4 downstream of a heliostat at elevation angle (a-c)  $\alpha = 0^\circ$ , (d-f)  $\alpha = 30^\circ$  and (g-i)  $\alpha = 60^\circ$ . Blue circles indicate the profiles in the wake of a single unmodified heliostat with no mesh and orange circles indicate the profiles in the wake of a single heliostat with a leading edge-mounted mesh device. The red dashed line indicates the heliostat hinge height  $z_h/c = 0.75$ .

Figure 11 shows the peak force coefficients on a heliostat with different edge-mounted mesh porosities of 0.9, 0.5 and 0.46 at a constant height-chord ratio  $h/c = 0.05$ , normalised with respect to those on an unmodified heliostat in Figure 4. The peak drag coefficient in Figure 11(a) at  $\alpha = 0^\circ$  increases with the addition of the mesh at all porosities, which is likely due to an increase in profile drag from the increased windward area due to the mesh. The increase in peak drag coefficient is minimised with the 0.46 porosity mesh device, particularly at  $\alpha = 0^\circ$  and  $30^\circ$ . The peak drag coefficient is most effectively reduced by 14% at  $\alpha = 30^\circ$  and by 7% at  $\alpha = 90^\circ$  with the 0.46 porosity mesh, suggesting that the influence of the mesh on flow separation opposes its effect on profile drag at operating angles. The 0.5 porosity mesh increases peak drag coefficient by 29% relative to an unmodified heliostat at  $\alpha = 0^\circ$  but notably produces a 5% reduction in peak drag coefficient at  $\alpha = 90^\circ$ , as the mesh reduces shedding of vortices from the lower edge of the heliostat. The mechanism behind the effect of the gap between the upright heliostat lower edge and the ground on drag coefficient warrants further investigation.

The peak lift coefficient in Figure 11(b) decreases marginally in stow position and at  $\alpha = 30^\circ$  with the addition of a mesh with 0.9 porosity. This indicates that a high-porosity mesh has a negligible influence on eddy behaviour and flow separation at low inclination angles. Lift coefficient at  $\alpha = 30^\circ$  decreases by 17% and 21% with the addition of 0.5 and 0.46 porosity meshes in Table 1, respectively, which indicates that flow separation is considerably reduced by a medium porosity (0.46 and 0.5) mesh at low elevation angles. At  $\alpha = 90^\circ$ , however, the peak lift coefficient increases by up to 10% in Table 1, which suggests unsteady interactions between a medium porosity mesh and the air flowing over the

edges of the heliostat in upright position. It is noted that the drag forces measured at  $\alpha = 0^\circ$  and lift forces measured at  $\alpha = 90^\circ$  are relatively small. Relative differences in the non-dimensional load coefficients have a higher uncertainty, as indicated by the increased size of the error bars in these cases, as they are close to the lower measurement range of the load cells.

As shown in Figure 11 and Table 1 a 0.46 porosity mesh is generally more effective at load reduction than the 0.9 porosity mesh. The mesh with 0.46 porosity meets the optimal value of porosity determined in experimentation on wind fence wake turbulence by Jafari *et al.* (2021). This lower porosity mesh becomes more effective at reducing lift, such as a 10% reduction in stow, and its performance at  $\alpha = 30^\circ$  is comparable with the 22% reduction observed by a 0.5 porosity mesh edge attachment relative to an unmodified heliostat. The favourable result of the 0.46 porosity mesh devices to reduce lift in stow position and at  $\alpha = 30^\circ$  is however compromised by increased drag in stow. Investigation of edge-mounted mesh devices with porosities smaller than 0.46 and their elevation with respect to the leading edge could further optimise the maximum wind loads and mitigate increases in drag.

Table 1. Peak wind load coefficients on unmodified heliostat with no mesh compared with a heliostat with edge-mounted mesh devices of different porosities and height-chord ratios.

Load configuration	Peak drag coefficient			Peak lift coefficient		
	$\alpha = 0^\circ$	$\alpha = 30^\circ$	$\alpha = 90^\circ$	$\alpha = 0^\circ$	$\alpha = 30^\circ$	$\alpha = 90^\circ$
Unmodified heliostat	0.50	1.47	2.78	0.52	2.17	0.42
Mesh porosity 0.46	0.52	1.27	2.58	0.47	1.72	0.43
Mesh porosity 0.5	0.64	1.35	2.66	0.54	1.79	0.46
Mesh porosity 0.9	0.54	1.46	2.63	0.49	2.12	0.45
Mesh $h/c = 0.1$	0.69	1.24	2.58	0.43	1.51	0.59
Mesh $h/c = 0.05$	0.52	1.27	2.58	0.47	1.72	0.43
Mesh $h/c = 0.025$	0.55	1.25	2.61	0.53	1.80	0.42

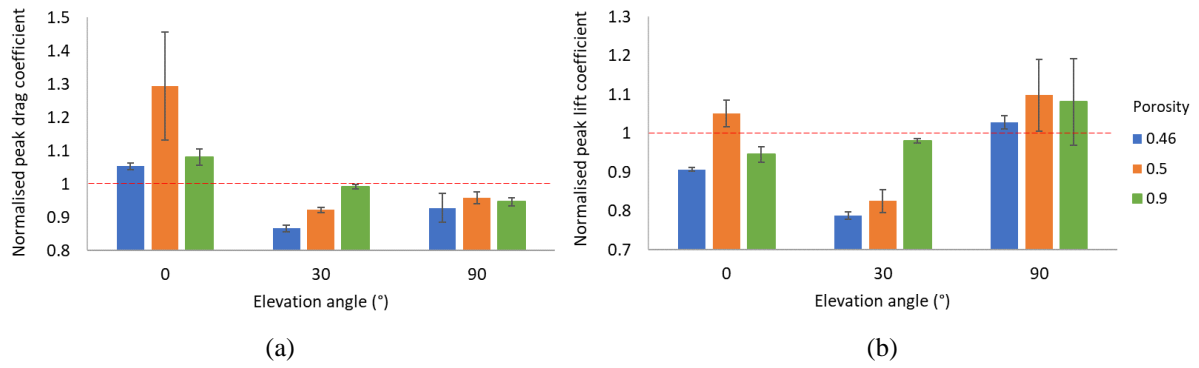


Figure 11. Effect of heliostat edge-mounted mesh grid porosity at different elevation angles on peak coefficient of (a) drag force and (b) lift force, compared with an unmodified heliostat. Error bars indicate the standard deviation calculated from three measurements.

Figure 12 shows the effect of a leading edge-mounted mesh with  $h/c = 0.1$ ,  $0.05$  and  $0.025$  at a constant mesh porosity of  $0.46$  on the peak drag and lift coefficients with respect to those on an unmodified heliostat in Figure 4. Increasing the height of the mesh from  $h/c$  of  $0.05$  to  $0.1$  appears to produce a net positive effect in terms of lift reduction due to the mesh. Lift coefficient at  $\alpha = 0^\circ$  with a mesh of  $h/c = 0.1$  is reduced significantly below that measured on an unmodified heliostat, by 16% in stow position and by 30% at  $\alpha = 30^\circ$  in Table 1. This corresponds to an approximate doubling of the lift reduction of that achieved with  $h/c = 0.05$ . Following the theory by Li and Sherman (2015), this is likely due to the increased height of the mesh being more effective at shielding the leeward regions of the heliostat. The increase in lift coefficient at  $\alpha = 90^\circ$  is comparable for the mesh devices with  $h/c = 0.05$  and  $0.025$ , however at  $\alpha = 90^\circ$  the peak lift coefficient is increased by 41% with  $h/c = 0.1$  in Table 1. The measured lift forces at  $\alpha = 90^\circ$  are relatively small and variations in lift forces in this case due to the addition of the edge devices have a higher uncertainty in the lower measurement range of the load cells, as demonstrated by the error bars in Figure 12. Peak drag is also increased by 38% in stow position by the taller mesh with  $h/c = 0.1$  in Table 1, likely due to the increased profile drag from the increased windward area. Drag at  $\alpha = 30^\circ$  is comparable over the range of  $h/c$  values tested, suggesting that the increased profile drag and decreased pressure drag oppose each other at intermediate elevation angles. Peak drag coefficients at  $h/c = 0.1$  and  $0.025$  in stow position show a pronounced increase when compared with a mesh device with  $h/c = 0.05$ . The peak lift coefficients in stow and at  $\alpha = 30^\circ$  follow a trend that favours increasing  $h/c$  of the mesh. Overall, the load reduction achieved with  $h/c = 0.025$  mesh is marginally smaller and quite comparable to the mesh with  $h/c = 0.05$  at the elevation



angles tested. This suggests that profile drag changes are negligible as the height of the mesh is dropped below  $h/c = 0.05$ .

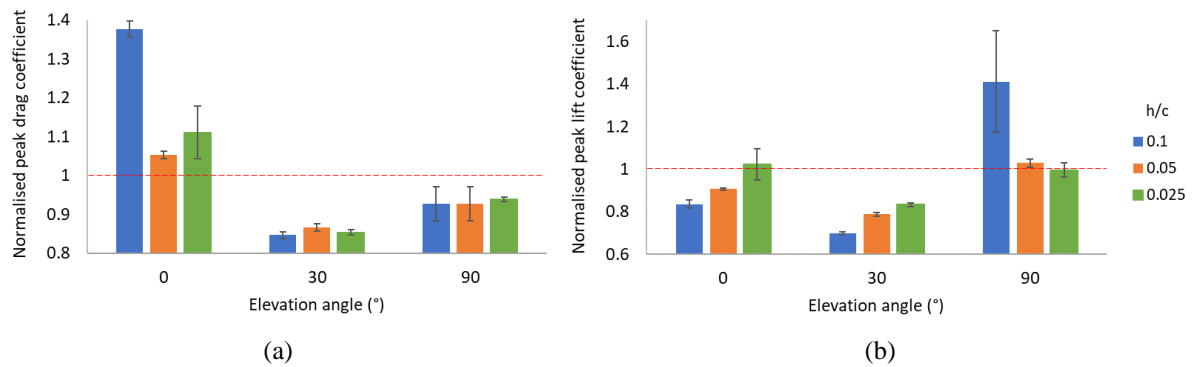


Figure 12. Effect of edge-mounted mesh height ratio with heliostat chord length ( $h/c$ ) at different elevation angles on peak coefficient of (a) drag force (b) lift force, compared with an unmodified heliostat. Error bars indicate the standard deviation calculated from three measurements.

## 4. Discussion

The radial spacing of heliostats in the rows of a field increases with increasing distance from the central tower. Maximum drag force and lift force reductions of 50% in operating positions and 55% in stow position, respectively, can be achieved on a single heliostat at 2.75 fence heights downstream of a 0.46 porosity fence. However, as shown in Figure 7 and Figure 8, the effect of a perimeter fence at all porosities tested diminishes with increasing distance to more than three fence heights downstream of the fence. Furthermore, favourable load reductions and the wake profiles show that the height of the fence should be scaled to be at least 25% higher than the operating maximum height of the heliostat surface. The use of perimeter fences to reduce wind loads on field-edge heliostats may therefore only be cost effective for smaller heliostats in regions of a heliostat field that are exposed to the prevailing wind direction. The optimal distance between the fence and the heliostats and a lower bound on the optimal porosity of a fence should be established with systematic investigations at a field scale.

Heliostat field perimeter fences are likely to have a smaller impact on wind loads with increasing distance in-field, as the sheltering effect of the fence becomes weaker and the flow within the field is strongly affected by the wake of upstream heliostats. An alternative approach to reduce loads at any position in a field has been investigated in the current study through heliostat edge-mounted mesh devices. Similar to perimeter fences, heliostat edge-mounted mesh devices with porosity less than 0.5 produce favourable reductions of 5-15% in peak operating drag force at  $\alpha = 90^\circ$ , 20-30% in peak

operating lift force at  $\alpha = 30^\circ$  and 5-10% in peak lift force at stow. However, these are opposed by increases in peak drag force in stow position ( $\alpha = 0^\circ$ ) and peak lift force in upright position ( $\alpha = 90^\circ$ ). Smaller variations in wind load relative to an unmodified heliostat are observed as the mesh height is reduced from  $h/c$  of 0.1 to 0.05 and presumably with further reduction in the mesh height. The favourable results in the current study, such as lift reduction at  $\alpha = 0^\circ$  and  $30^\circ$  and drag reduction at  $\alpha = 90^\circ$ , indicate that small-sized heliostats can be made lighter if properly configured at the perimeter of a field. The viability of using edge-mounted mesh devices on inner-field heliostats warrants further testing and consideration of blocking and shading of the reflective surface.

The impact of the wind load reductions reported in the current study due to an edge-mounted mesh device on the cost of a heliostat can be estimated using ABL turbulence-load correlations and stress analysis equations in Emes *et al.* (2020). The changes in peak drag and lift coefficients due to the edge-mounted mesh device with 0.46 porosity, compared with an unmodified heliostat in the current study, are shown in Table 2. For a 25 m<sup>2</sup> square heliostat ( $c = 5$  m) with constant 5 mm thickness of steel structural components and assumed elevation axis height of 3 m, the load coefficients in Table 2 and equations 15-19 in Emes *et al.* (2020) were used to estimate the maximum wind loads in operating and stow positions. The minimum outer diameter of a constant thickness pedestal and torque tube to resist the combined von Mises stress due to bending and torsional stresses under different wind load configurations were calculated using equations 2-12 in Emes *et al.* (2020), respectively, and an assumed steel cost of \$2/kg (Emes *et al.* 2020). The addition of the edge-mounted mesh device on a 25 m<sup>2</sup> heliostat was estimated to reduce the pedestal cost by 1-3% and reduce the torque tube cost by 4-10% depending on the stow and operating load configurations. This indicates the potential of edge-mounted mesh devices on heliostats in a field to mitigate turbulence effects and reduce wind loads on heliostats in the near or far field where the elevation angles approach  $90^\circ$  and  $0^\circ$ , respectively. A systematic techno-economic analysis of the cost of application of edge-mounted mesh devices on full-scale heliostats and their sensitivity and impact to neighbouring rows of a heliostat field would be of benefit to demonstrate feasibility of such devices as a substitute or complement of existing fences at the perimeter of a field.

Table 2. Changes in heliostat load coefficients due to an edge-mounted mesh device with 0.46 porosity.

Load configuration	Peak drag coefficient			Peak lift coefficient		
	$\alpha = 0^\circ$	$\alpha = 30^\circ$	$\alpha = 90^\circ$	$\alpha = 0^\circ$	$\alpha = 30^\circ$	$\alpha = 90^\circ$
<b>Heliostat</b>	0.50	1.47	2.78	0.52	2.17	0.42
<b>Heliostat with mesh</b>	0.52	1.27	2.58	0.47	1.72	0.43
<b>Difference</b>	+4%	-14%	-7%	-10%	-21%	+3%

## 5. Conclusions

This paper quantified the force reduction on a single heliostat at a range of operating conditions through a sensitivity analysis of the scaling parameters of perimeter mesh fences and edge-mounted mesh devices. It was found that an optimal mesh fence porosity of 0.46 resulted in maximum drag force and lift force reductions in the range of 50-55% on a heliostat in the first row of a field. The distance between the fence and the heliostat also affected the loads on the heliostat. Porosity and height-chord ratio of an edge-attachment mesh were found to be important parameters influencing the maximum drag and lift reductions in operating and stow positions. Peak drag and lift coefficients on an operating heliostat at  $\alpha = 30^\circ$  were reduced by up to 15% and 30%, respectively, with decreasing porosity and increasing height-chord ratio of the mesh device. The peak stow lift coefficient was reduced by up to 10% with decreasing porosity of the mesh device to 0.46, however the opposite effect of the mesh device was observed with increases in peak drag coefficient in stow position and peak lift force at  $\alpha = 90^\circ$ . Hence, there is a trade-off between wind loads at different elevation angles that impacts the mesh effectiveness in reducing wind load and cost of heliostat structural components. Systematic investigation through field-scale testing and techno-economic analysis is warranted to assess the sensitivity of wind load reduction on a heliostat in stow and operating positions to perimeter fence and edge-mounted mesh devices with their porosity, height, and longitudinal distance.

## Acknowledgements

The authors would like to thank the Australian Solar Thermal Research Institute (ASTRI) for their support with funding provided by Australian Renewable Energy Agency (ARENA) Grant 1-SRI002.

## References

- Department of Energy (2017), “The SunShot 2030 Goals”, DOE/EE-1501; Solar Energy Technologies Office, USA.
- Emes, M., Jafari, A., Pfahl, A., Coventry, J. and Arjomandi, M. (2021), A review of static and dynamic heliostat wind loads, *Solar Energy*, 225, 60-82.
- Emes, M.J., Arjomandi, M., Ghanadi, F. and Kelso, R.M. (2017), Effect of turbulence characteristics in the atmospheric surface layer on the peak wind loads on heliostats in stow position, *Solar Energy*, 157, 284-297.
- Emes, M.J., Jafari, A., Coventry, J. and Arjomandi, M. (2020), The influence of atmospheric boundary layer turbulence on the design wind loads and cost of heliostats, *Solar Energy*, 207, 796-812.
- Emes, M.J., Jafari, A., Ghanadi, F. and Arjomandi, M. (2019), Hinge and overturning moments due to unsteady heliostat pressure distributions in a turbulent atmospheric boundary layer, *Solar Energy*, 193, 604-617.
- Jafari, A., Emes, M., Cazzolato, B., Ghanadi, F. and Arjomandi, M. (2021), Wire mesh fences for manipulation of turbulence energy spectrum, *Experiments in Fluids*, 62(2), 30.
- Jafari, A., Ghanadi, F., Arjomandi, M., Emes, M.J. and Cazzolato, B.S. (2019), Correlating turbulence intensity and length scale with the unsteady lift force on flat plates in an atmospheric boundary layer flow, *Journal of Wind Eng and Ind Aero*, 189, 218-230.
- Jafari, A., Ghanadi, F., Emes, M.J., Arjomandi, M. and Cazzolato, B.S. (2019), Measurement of unsteady wind loads in a wind tunnel: scaling of turbulence spectra, *Journal of Wind Eng and Ind Aero*, 193, 103955.
- Li, B. and Sherman, D.J. (2015), Aerodynamics and morphodynamics of sand fences: A review, *Aeolian Research*, 17, 33-48.
- Perera, M. (1981), Shelter behind two-dimensional solid and porous fences, *Journal of Wind Engineering and Industrial Aerodynamics*, 8(1-2), 93-104.

- Peterka, J.A. and Derickson, R.G. (1992), “Wind load design methods for ground-based heliostats and parabolic dish collectors”, SAND92-7009; Sandia National Laboratories, Albuquerque, New Mexico.
- Peterka, J.A., Hosoya, N., Bienkiewicz, B. and Cermak, J.E. (1986), “Wind load reduction for heliostats”, SERI/STR-253-2859; Colorado State University, Fort Collins, USA.
- Peterka, J.A., Tan, Z., Cermak, J.E. and Bienkiewicz, B. (1989), Mean and peak wind loads on heliostats, *Journal of Solar Energy Engineering*, 111(2), 158-164.
- Pfahl, A. (2018), *Wind loads on heliostats and photovoltaic trackers*, PhD Thesis, Eindhoven University of Technology, Eindhoven, Netherlands.
- Pfahl, A., Brucks, A. and Holze, C. (2014), Wind load reduction for light-weight heliostats, *Energy Procedia*, 49, 193-200.
- Pfahl, A., Randt, M., Meier, F., Zashke, M., Geurts, C. and Buselmeier, M. (2015), A holistic approach for low cost heliostat fields, *Energy Procedia*, 69, 178-187.
- Teruna, C., Avallone, F., Casalino, D. and Ragni, D. (2021), Numerical investigation of leading edge noise reduction on a rod-airfoil configuration using porous materials and serrations, *Journal of Sound and Vibration*, 494, 115880.